

The Eastern Arm of M83 Revisited: High-Resolution Mapping of ^{12}CO 1-0 Emission

Richard J. Rand

Dept. of Physics and Astronomy, University of New Mexico, 800 Yale Blvd, NE, Albuquerque,
NM 87131

Steven D. Lord

Infrared Processing and Analysis Center, MS 100-22, California Institute of Technology,
Pasadena, CA 91125

and

James L. Higdon

Kapteyn Astronomical Institute, University of Groningen, Postbus 800, 9700 AV Groningen, The
Netherlands

ABSTRACT

We have used the Owens Valley Millimeter Array to map ^{12}CO ($J=1-0$) along a 3.5 kpc segment of M83's eastern spiral arm at resolutions of $6.5'' \times 3.5''$, $10''$, and $16''$. The CO emission in most of this segment lies along the sharp dust lane demarking the inner edge of the spiral arm, but beyond a certain point along the arm the emission shifts downstream from the dust lane to become better aligned with the young stars seen in blue and $H\beta$ images. This morphology resembles that of the western arm of M100. Three possibilities, none of which is wholly satisfactory, are considered to explain the deviation of the CO arm from the dust lane: heating of the CO by UV radiation from young stars, heating by low-energy cosmic rays, and a molecular medium consisting of two (diffuse and dense) components which react differently to the density wave. Regardless, the question of what CO emission traces along this spiral arm is a complicated one. Masses based on CO emission and the virial theorem for ten emission features roughly agree and are in the range $1.5\text{--}16 \times 10^6 M_{\odot}$. These are lower than the masses of GMAs in M51, but the discrepancy is probably due to the much higher linear resolution of these observations. Despite the uncertainty in what CO emission is tracing, we do not require a conversion factor of CO brightness to H_2 column density much different from the standard Galactic value if these structures are bound. Surprisingly, for the two fields where we can compare with single-dish data, only 2-5% of the single-dish flux is seen in our observations. A possible explanation is that M83 contains much smoothly distributed molecular gas that is resolved out by the interferometer. Strong tangential streaming is observed where the arm crosses the kinematic major axis of the galaxy, implying that the shear becomes locally

prograde in the arms. The amplitude of the tangential streaming is used along with a low-resolution single-dish radial profile of CO emission to infer a very high gas surface density of about $230 \text{ M}_{\odot} \text{ pc}^{-2}$ and an arm-interarm contrast greater than 2.3 in the part of the arm near the major axis. Using two different criteria, we find that the gas at this location is well above the threshold for gravitational instability – much more clearly so than in either M51 or M100. This finding is consistent with the unusually high $\text{H}\alpha$ surface brightness and star formation efficiency in M83: star formation may be particularly active because of strong gravitational instabilities.

Subject headings: galaxies: individual (M83): — galaxies: interstellar matter — galaxies: evolution — radio lines: galaxies — interstellar: molecules

1. Introduction

M83 is one of the brightest known galaxies in terms of molecular emission [$I_{\text{CO}} = 64 \text{ K km s}^{-1}$ over the inner 2 kpc; Lord (1987)], and is the nearest ($D = 5 \text{ Mpc}$) barred spiral. It is also notable for its large angular size ($D_{25} = 12.9'$), its large and massive bar, and high star formation rate ($5 \text{ M}_{\odot} \text{ yr}^{-1}$; Kennicutt, Tamblyn, & Congdon 1994). Other global properties are summarized in Table 1.

The eastern arm in particular has been popular for studies of star formation and spiral density wave dynamics because it shows a clearly delineated dust lane bordering a grand design spiral arm (Figure 3, Plate 00, top left panel). A series of detailed studies of this region began with Allen et al. (1986), who argued that compression of the molecular gas in the spiral shock at the dust lane is triggering star formation. About 400 pc ($15''$) towards the concave or outer edge of the arm (i.e. the downstream edge assuming a trailing arm inside the corotation radius of the spiral density wave; under this assumption, rotation proceeds clockwise), newly-formed stars photodissociate the H_2 in GMCs and produce the HI ridge found along the optical arm.

However, Wiklind (1990), and Lord & Kenney (1991; hereafter LK) found evidence to the contrary: CO observations of the southern part of this arm showed that the molecular emission does not peak at the dust lane but instead downstream at the very sites where Allen et al. would have a significant fraction of cloud H_2 mass converted to HI. The results suggest that UV illumination could highlight molecular clouds close to newly-formed stars by elevating cloud temperatures, and thus that CO emission does not reflect the true distribution of molecular gas. However, LK argued that UV heating of clouds in the arm alone is incapable of producing all of the observed CO emission. Rather, cloud compression in the optical arm (rather than in the dust lane) is suggested.

A simpler picture can be drawn for M51, where the excellent coincidence of the CO emission and the dust lanes throughout the galaxy implies that CO is a good tracer of molecular gas column

density (Vogel, Kulkarni, & Scoville 1988; Rand & Kulkarni 1990; Gruendl 1996). The HI is associated with the arms of HII regions, generally downstream from the CO arms and dust lanes, and thus can be naturally explained as a dissociation product (Tilanus 1990; Rand, Kulkarni, & Rice 1992). In the western arm of another grand-design spiral, M100, Rand (1995) found that CO is coincident with the dust lane at the beginning of the arm, but further along it becomes better aligned with star forming regions (Rand 1995).

A possible explanation for such varying morphologies is that in CO-luminous galaxies like these three, much of the diffuse ISM may be in molecular form (Elmegreen 1993). Collision fronts for diffuse and dense gas in general need not occur at the same place in a spiral arm, depending on the strength of the density wave (Elmegreen 1988). If the wave is sufficiently weak, only diffuse gas is trapped at the well-organized shock front marked by the dust lane on the inner edge of a spiral arm. The dense clouds (i.e. GMCs), orbiting quasi-ballistically in a manner similar to the stars, can pass through the shock front and form a broad ridge centered on the spiral arm. The GMCs would be responsible for the CO emission. In this interpretation, the strong density wave in M51 is capable of compressing both the diffuse and dense molecular components at the shock front, accounting for the excellent coincidence of CO emission and the dust lanes. In M100, the density wave would have to weaken sufficiently with distance along the spiral arm so that both molecular components are trapped at the shock front at the beginning of the arm but only the diffuse component further along the arm. In this explanation, the shock front at the location investigated by LK would also be relatively weak.

Deutsch & Allen (1993) argue for a third possibility to explain the CO emission downstream from the dust lane: low-energy *cosmic ray heating* (see also Adler, Allen, & Lo 1991; Suchkov, Allen, & Heckman 1993). They have produced a non-thermal radio continuum map of M83 (from a 20-cm map and an extinction-corrected $H\beta$ image used to estimate the thermal component) at 10" resolution which shows a ridge of emission well aligned with the dust lane along most of the eastern arm but shifts away from it in the southern part to become better aligned with the small CO features found by LK. They suggest that the mid-arm ridge is bright in CO due to cosmic ray heating brought on by frequent supernovae, and not due to a gas density enhancement. They predict that enhanced CO emission should generally occur along this ridge. Testing their model against observations of M51, they argue that the CO arms are coincident with the dust lanes primarily because the non-thermal emission peaks there too (see also Tilanus et al. 1988). The fundamental correlation, then, is claimed to be not between CO and dust but between CO and non-thermal emission. If true, we are faced with the uncomfortable proposition that CO emission largely traces the effects of cosmic-ray heating rather than the molecular mass distribution, at least in some parts of spiral arms. This has obvious consequences for our understanding of such topics as the growth of molecular clouds and star formation.

Determining which of these mechanisms - UV heating, cosmic-ray heating, and selective compression of dual molecular gas components - is dominant in M83's arms has not been possible due to the lack of CO maps of sufficient sensitivity, resolution, and coverage to provide good

observational tests. Hence, one of the main goals of the more extensive mapping of CO in the eastern arm presented here is to probe this issue further.

A second reason to study this arm further is to understand the dynamical process of star formation in spiral density wave compressions. For M51 (Rand 1993b) and M100 (Knapen et al. 1996), it has been found that the efficiency of star formation is higher in the arms than in the interarm regions. One possible reason is that the arms are conducive to large scale gravitational instability in the gas, as discussed by (e.g.) Kennicutt (1989) and Elmegreen (1994). Applying theoretical criteria from these studies to the observations indicates (Rand 1993b; Rand 1995) that the gas surface density in the spiral arms in both galaxies is indeed somewhat above the threshold for the onset of instabilities, while interarm gas hovers near the threshold values, at least in the parts of the galaxies where arm and interarm surface densities can be determined by the kinematic method described in §3.5. These comparisons, of course, depend on CO being a fair tracer of molecular gas, encapsulated in a global relation between CO emission and H₂ column density – the X factor. If X is lower by a factor of two or three than the Galactic or “standard” value of $X_{Gal} = 2.8 \times 10^{20} \text{ mol cm}^{-2} (\text{K km s}^{-1})^{-1}$ in these galaxies, as hinted at by some studies (Rand 1993a; Adler et al. 1992; Nakai & Kuno 1995; Rand 1995), then the gas in the arms would be at about the threshold surface density. In M83 as well, there must be some doubt about the X factor given the uncertain interpretation of the CO emission as discussed above.

Measures of star formation rates, surface densities, and global efficiencies for the galaxies M83, M51, and M100 are shown in Table 2. All molecular masses assume X_{Gal} and are defined for the regions listed in the footnote. While these masses are lower limits because the outer regions of the galaxies have not been mapped, it is unlikely that a large fraction of their H₂ masses lies outside these areas. The H α luminosity of M83 is comparable to that of M100 and M51, but the surface density of H α emission is much higher in M83 and M51 than in M100. Also, M83’s global star formation efficiency, defined observationally as $L_{H\alpha}/M_{H_2}$, is about 2.5 times that of M51 and more than 3 times that of M100, subject to uncertainties in X . It is an important open question whether these apparent variations in SFE can be related to levels of gravitational instability in the molecular gas from one galaxy to the next.

To summarize, in this study we hope to further our understanding of CO emission and the star formation process in galaxies by mapping a much larger segment of the eastern arm of M83. We would like to understand in general the degree to which the CO emission reflects compression in a density wave, cosmic ray heating, or UV heating from newly formed stars. Specifically, we focus on the mystery of the differences between M83, M51 and M100. Does the CO in M83 generally coincide better with the dust lane, the young stars or the non-thermal emission? We also wish to understand how the density wave compression raises the molecular gas surface density in M83, especially in comparison with M51 and M100, and we will apply the aforementioned criteria for gravitational instability to see whether the very high surface density of star formation may be due to gas highly prone to gravitational collapse.

2. Observations

Four fields along M83's eastern arm were imaged with the six-element Owens Valley Radio Observatory (OVRO) Millimeter Array. With pointings separated by about $40''$ (primary-beam $\theta_{FWHM} = 65''$ at 115 GHz), there is significant overlap between the fields (see the dashed circles in Figure 2). The observed region runs along the arm starting at the northern end of the central bar, and extending about $2.5'$ (3.5 kpc) to the south. The region was specifically chosen to cover the area studied by Deutsch & Allen (1993) and the other works mentioned above. Attention was paid to arrange the fields to sample the sharp dust lane and to include the full width of the spiral arm.

Offsets of the pointing centers of the four fields from the center of the galaxy are shown in Table 3. The fields were observed between December 1995 and June 1997 in three different configurations with baselines ranging in length from 15 to 85 m, providing good uv coverage for low-declination sources. The quasar 1334-127 was used to correct for temporal amplitude and phase variations. The flux standard for the maps was primarily determined through observations of Neptune, while for some tracks the sources 3C273 and 3C345 were used. These quasars were also used for bandpass calibration. Spectral coverage was provided by 32 1-MHz correlator channels resulting in a resolution of 2.6 km s^{-1} and an instantaneous bandwidth of 83.2 km s^{-1} . Naturally weighted channel maps separated in velocity by 5.2 km s^{-1} were made and CLEANed using NRAO's¹ AIPS software package.

The resulting synthesized beam FWHM was $6.5'' \times 3.5''$ (P.A. = -10°), which at the assumed distance of 5 Mpc corresponds to a linear resolution of $160 \times 85 \text{ pc}$. There were slight variations in resolution from field to field. Structures as large as $\sim 30''$ (750 pc) should be well imaged. The 1σ map noise for each field in 5.2 km s^{-1} channels is listed in Table 3. The four cubes were linearly mosaicked together and corrected for primary beam attenuation using the task "linmos" in the MIRIAD package (Sault, Teuben, & Wright 1995). Primarily for the purpose of examining the velocity field, maps of each field at about $10''$ resolution were made by tapering the uv data (again there is a slight variation in resolution from field to field), and a mosaic cube was formed from these. A mosaic cube at $16''$ resolution was also produced by convolving the $10''$ -resolution mosaic cube with a Gaussian to match the *linear* resolution of the observations of M51 by Rand & Kulkarni (1990). Integrated line intensity and velocity field maps were made by first masking emission free regions in the channel maps, and then using only those pixels with signals exceeding a specified ($1.5 - 2\sigma$) noise level.

Although the map of non-thermal emission by Deutsch & Allen (1993) provides a useful comparison with the CO data, their original Very Large Array (VLA) 20-cm continuum map has considerably lower resolution ($10''$) than our CO map. In order to compare the CO and 20-cm

¹The National Radio Astronomy Observatory is operated by the Associated Universities, Inc. under cooperative agreement with the National Science Foundation.

distributions at matched resolutions, we made new *robust* weighted maps using the VLA B-array data provided by J. Cowan (cf. Cowan, Roberts, & Branch 1994). Setting the “robust” parameter to -0.2 in the AIPS task IMAGR gave final CLEANed maps with synthesized beams nearly matching the OVRO data ($7.0'' \times 3.4''$), with only a $\sim 10\%$ increase in the map noise ($40 \mu\text{Jy beam}^{-1}$) over natural weighting. The wide range in baselines ensured that emission structures as large as $\sim 100''$ would still be well imaged. Note that we have not attempted to remove a thermal component from this map.

3. Results

3.1. General Morphology and Comparison with Other Tracers

Figure 1 shows the channel maps from the full-resolution cube for the velocity range of $427.6\text{--}516.0 \text{ km s}^{-1}$. The full-resolution map of total CO intensity is shown in Figure 2. Figure 3 shows overlays of CO contours on other spiral tracers: (top left panel) a blue CCD image; (top right) the 20-cm map; (bottom left) an $\text{H}\beta$ image from Tilanus & Allen (1993; hereafter TA); and (bottom right) a three-color image in which blue, red, and green represent CO, 20-cm, and $\text{H}\beta$ emission, respectively.

Figure 2 clearly shows a segment of a molecular spiral arm, with much substructure. The relationship between the CO emission and the dust lane revealed by the blue CCD image in Figure 3 is very complex. At the beginning of the mapped part of the arm, there is a noticeable bifurcation of the dust lane at R.A. $13^{\text{h}} 34^{\text{m}} 15^{\text{s}}$, Dec. $-29^{\circ}36'10''$. These two lanes appear to merge again at about R.A. $13^{\text{h}} 34^{\text{m}} 18.5^{\text{s}}$, Dec. $-29^{\circ}36'30''$. There are also patches of extinction between these two lanes. In this region, the CO mainly coincides with the prominent outer dust lane, although faint emission can be seen at the beginning of the inner dust lane as well. South of where the lanes join again, there is good coincidence of the CO emission and the dust lane. However, at about Dec. $-29^{\circ}37'$, the CO emission deviates from the main dust lane and becomes more coincident with the young stellar clusters downstream, although at least two CO clumps are still associated with the prominent dust lane. This part of the arm includes the region mapped by LK and the current map confirms their finding of an offset while revealing much more information about the CO-dust relationship. We will often refer to this part of the arm as the “southern segment,” and the part further to the north where CO and dust are more coincident as the “northern segment.” To the degree that CO shows general alignment with the dust lane at the beginning of the arm but better alignment with star formation further along the arm, the eastern arm of M83 resembles the western arm of M100 mapped by Rand (1995). This general CO-dust morphology was predicted by LK.

Despite their prominence, the dust lanes in the southern segment do not show substantial detectable CO emission. However, by our estimates this is not surprising. From the excess extinction ($A_B = 0.9$) LK inferred a corresponding gas column density of $\sim 5 \times 10^{21} \text{ mol cm}^{-2}$.

A cloud with this average column density would have a CO brightness of $\sim 2 \text{ K km s}^{-1}$, assuming X_{Gal} . For a triangular line profile with a FWHM of 8 km s^{-1} , the peak brightness would be 0.3 K. Our 1σ sensitivity in the channel maps is 0.2 K at full-resolution and 0.1 K at $10''$ resolution. Hence, a cloud of this column density, reasonably well matched to the beam size, would be a marginal detection in our maps. Detectability is improved if the gas is clumped. We do see one feature (No. 10 in Figure 2) on the dust lane in the southern segment, with an average column density of about $2 \times 10^{21} \text{ mol cm}^{-2}$.

As an aside, in Wiklind's (1990) SEST map of part of the eastern arm (overlapping our fields 2, 3, and 4) CO is again generally associated with the optical arm. However, this result by itself does not rule out a faint narrow ridge of molecular gas along the dust lane. Such a ridge may be so smoothed out by the $43''$ beam that it cannot be distinguished from the broader CO emission from the optical arm.

So perhaps it is not so surprising that CO emission is difficult to detect on this segment of the dust lane. On the other hand, LK estimate that the extinction in the dust lane in M51's northwest arm is about half the above value, yet CO emission is readily detectable. However, LK also conclude that M51's dust lane – and by implication the molecular distribution – is clumpier than M83's, making it more easily detectable interferometrically. Indeed, the dust lane in the northern segment of the M83 arm appears to be patchier than the southern segment lane. Additional uncertainty in the comparison is in the relative vertical distributions of stars and dust in the arms of the two galaxies – there may be much hidden dust in some regions.

Figure 4 shows CO contours on the non-thermal radio emission map of Deutsch & Allen (1993). Comparison of the CO distribution with the two radio continuum maps in Figures 3 and 4 give somewhat different impressions, but both show a complicated spatial relationship. In Figure 4, a rather broad non-thermal arm can be seen, surrounded by lower-level emission. Much of the beginning of the northern CO segment generally lies along the northern edge of the non-thermal arm, but some CO emission extends northward into the low-level non-thermal emission. Further to the west and south, the coincidence is much better. Interestingly, at the top of the southern segment where the CO arm shifts away from the dust lane towards the young stellar clusters, the non-thermal arm shows the same behavior. Further down this segment, the non-thermal arm tends to wander back and forth across the CO arm. One limitation of this non-thermal map is that the thermal component was estimated from an $H\beta$ image. If there is patchy extinction and the estimated thermal fraction is large enough then the non-thermal map calculated in this way could show small-scale differences from the true distribution of emission. A non-thermal map produced from multi-frequency radio observations should provide a more robust comparison.

The 20-cm map in Figure 3 shows, in the northern segment, a few bright peaks of emission along the top edge of the still-present broad arm. These form a ridge somewhat coincident with the CO arm. However, there are several CO peaks which do not have associated continuum peaks, and some CO emission still extends northward of this ridge. Also, the three brightest 20-cm peaks

coincide with HII regions (see the three-color image), and may therefore have a substantial thermal component. Again, high-resolution multi-frequency radio observations could resolve this issue. Finally, there is little CO emission associated with the lower-level broad arm of 20-cm emission, despite the fact that this arm overlaps the southern bifurcation of the dust lane. In the southern segment two peaks of CO and 20-cm emission coincide, but on scales close to the resolution the correlation is not good.

Figure 3 shows that the relation between CO and $H\beta$ emission is also rather complex, and again shows many similarities to M100. In the northern segment, CO is generally found at the inner edge of the $H\beta$ arm. In other words, there is no systematic offset of CO and the most luminous HII regions as is the case in M51, but much more $H\beta$ emission is found downstream of the CO than upstream, as seen in the northern segment of the western arm of M100. As explained by Rand (1995), this morphology is still consistent with triggered star formation in a molecular compression (as long as CO emission traces the compression), but if there is any time delay between the compression of the gas and the onset of massive star formation, it does not lead to a large CO- $H\beta$ offset. This can happen if the delay is rather short, if star formation is not precisely sequenced along the arm, or if the velocity component perpendicular to the arm of the gas flow vector is sufficiently small. On smaller scales, patches of CO emission are sometimes coincident with HII regions, sometimes not. In the southern segment, the CO arm is coincident with the middle of the $H\beta$ arm, which is delineated by luminous HII regions, again very similar to the M100 case. The small-scale correlation of CO and $H\beta$ peaks is again poor.

A comparison of Figure 17 of TA with Figure 3 shows that there is no clear systematic offset between M83's HI and CO arms. Only in Field 2 (roughly between Declinations $-29^{\circ}35'45''$ and $-29^{\circ}36'45''$) can it be said that HI is found preferentially downstream of CO. On the other hand, given the lack of a clear CO- $H\beta$ offset even in the northern segment, it may still be the case that the HI is produced by dissociation of H_2 by newly formed stars. The dissociation picture is difficult to establish when spatial offsets are not clear, let alone the origin of the CO emission.

3.2. Fraction of Single-dish Flux Recovered

Lord (1987) measured a line flux of $1300 \text{ Jy km s}^{-1}$ with the FCRAO 14-m telescope near the center of our Field 1 (Table 1). Within an area equal to the FCRAO beam ($45''$) we detect 30 Jy km s^{-1} , or only about 2% of the single-dish flux. LK similarly observed their field using the NRAO 12-m telescope and measured a line flux of 357 Jy km s^{-1} . Over the corresponding single-dish beam area ($65''$) we measure 18 Jy km s^{-1} , or again only a small fraction (5%) of the total line flux. These recovered fractions are much lower than in interferometric observations of other spirals: e.g. 35% for OVRO observations of M51 (Rand & Kulkarni 1990) and 55% for BIMA observations of M100 (Rand 1995). A contributing factor may be the combination of a small synthesized beam and the relative proximity of M83, leading to a linear resolution of only $\sim 100 \text{ pc}$. The 400-pc and 600-pc linear resolutions of the M51 and M100 observations,

respectively, may be better matched to the width of the molecular spiral arms, leading to a larger recovered fraction of the flux.

On the other hand, in two recent interferometric studies of another nearby grand-design spiral M81 (Taylor & Wilson 1998; Brouillet et al. 1998), with beam sizes of about $3''$ (45 pc for $D = 3$ Mpc) and $5''$ (75 pc) respectively, a majority of the single-dish flux was recovered. Perhaps in CO-rich galaxies such as M83, M51, and M100, the molecular gas is relatively widespread on scales larger than GMCs (such as GMA, spiral arm, and galaxy-wide scales), while in a CO-poor galaxy such as M81, the molecular gas is concentrated into relatively small, GMC-sized units embedded in a sea of HI, making it possible to recover most of the emission despite the spatial filtering of an interferometer.

3.3. Properties of Discrete Emission Features

The CO emission along the spiral arm is very clumpy, with many features standing out as well-defined peaks, while other parts show more smoothly distributed emission. The features which are bright and distinct enough to allow an accurate measurement of their fluxes, sizes and linewidths are labeled in Figure 2. We compute masses based on CO flux and on the virial theorem for these features. Of course, for the former mass estimates, we assume that CO emission is a fair tracer of molecular column density – an assumption that may be questionable given our lack of understanding of CO excitation in this galaxy.

Masses based on CO flux, M_{CO} , are calculated from the full-resolution map using the following formula:

$$M_{CO} = 3.3 \times 10^5 \frac{F}{(\text{Jy km s}^{-1})} \left(\frac{D}{5 \text{ Mpc}} \right)^2 \frac{X}{X_{Gal}}, \quad (1)$$

where F is the integrated flux from the GMA, and D is the distance to M83. Values of M_{CO} are listed in Table 4 for $X = X_{Gal}$.

Uncertainties arise from the assumed distance, the conversion factor adopted, and the flux calibration. The distance is assumed to be 5 Mpc, but values as low as 3.7 (de Vaucouleurs 1979) and as high as 8.9 Mpc (Sandage & Tammann 1975) have been used. Conservatively using these extremes as an indication of the uncertainty in that quantity, the fractional uncertainty from flux calibration and distance considerations alone is 1.0. We will return to the question of the value of X after comparing these masses with virial masses.

We calculate the virial mass in the same way as Rand (1995):

$$M_{vir} = 550 d (\sigma_{1d})^2 M_{\odot} \quad (2)$$

where d is the deconvolved diameter and σ_{1d} is the 1-d velocity dispersion. The latter is estimated from the measured FWHM of the line profile averaged over the area of the feature. Most of

the features are resolved and we use the geometric mean of their sizes to calculate d . The formal uncertainties in M_{vir} are due to the distance uncertainty and the approximately 2 km s^{-1} uncertainty in the estimated FWHM of the spectra. In general, the virial masses are quite comparable to the flux-based masses given the large uncertainties, with the main exceptions being features 8, 9, and 10.

The range of masses extends from the equivalent of the largest Galactic GMCs (e.g. Scoville & Sanders 1987) to the smaller GMAs of M51 (Rand & Kulkarni 1990). If these features are really bound units, then the assumed value of X must be reasonable. However, from recent studies of other nearby spirals, one could make an argument that the appropriate value of X may be two or three times lower than assumed. M83 has a high oxygen abundance: six HII regions in M83 have been studied by Dufour et al. (1980), with three of these in a range of galactocentric radii similar to that of the CO emission. They have abundances of $12 + \log(\text{O}/\text{H}) = 9.64, 9.54$, and 9.43 . For M51, a galaxy with an oxygen abundance as high as that of M83 (Dufour et al. 1980), a value of X three times lower than the standard Galactic value is hinted at by Rand (1993a), Adler et al. (1992), and Nakai & Kuno (1995). Wilson (1995) finds from a comparison of CO-based and virial masses of GMCs in five Local Group galaxies (IC 10, M31, M33, NGC 6822, and the SMC) that X increases by a factor of 4.6 as the oxygen abundance decreases by a factor of 10. While Wilson (1995) does not include galaxies with abundances as high as M83 or M51, extrapolation of her relationship would also indicate a value of X about three times below the Galactic value. Obviously, such an extrapolation is dangerous, and theoretically at least, while a dependence of X on abundance is expected, it is predicted to be weak for abundances above solar (Maloney & Black 1989). Adoption of the lower value of X would cause the majority of the features found here to be unbound. While possible, this conclusion would challenge the idea, developed from observations of several nearby spirals, that galaxies with high molecular contents and strong density wave compressions should be able to grow larger bound units. At this point, then, there is currently no compelling reason to assume a significantly lower value of X .

Apart from their boundedness, why do we not see features as massive as in M51? It is no doubt the case that the typical size of features seen is an effect of resolution. Because of M83's relative proximity and the high angular resolution of the observations, we tend to see smaller structures than in M51 [note that even larger features were found in M100 by Rand (1995), where the linear resolution was about 600 pc]. Discrete features at this linear resolution ($160 \times 85 \text{ pc}$) will blend together when observed at the 370-pc resolution of the M51 observations of Rand & Kulkarni (1990). To demonstrate this, we examine a total-intensity map made from the $16''$ -resolution cube, which was created to match the linear resolution of the M51 observations. It shows only four discrete clumps, each an association of two or three of the features observed at full resolution. Their flux-based masses, using X_{Gal} , are now in the range $1.1 - 4.3 \times 10^7 M_{\odot}$ - more comparable to the typical $3 \times 10^7 M_{\odot}$ mass of the GMAs in M51.

Interestingly, though, the virial masses are generally much higher than the flux-based masses - in the range $5.9 - 27 \times 10^7 M_{\odot}$ - mainly due to the rather large line-widths (two are strictly

upper limits due to being spatially unresolved, but from the full-resolution map it can be inferred that their sizes should be comparable to the $16''$ beam). Hence, at this resolution, they appear as unbound GMAs. A lower X would worsen the discrepancy [whether the arm GMAs in M51 are unbound is complicated by the fact that many are unresolved (Rand & Kulkarni 1990) as well as the uncertain value of X].

3.4. Kinematics and Streaming Motions

It was concluded by TA from analysis of VLA HI and Fabry-Perot $H\beta$ velocity fields that density wave induced streaming motions are much weaker in M83 than in M51. After subtraction of a rotation curve (derived from the HI data) which rises linearly to 185 km s^{-1} at $R = 2.5'$ and is flat beyond this radius, they found at most a suggestion of a 15 km s^{-1} (in the plane of the sky) velocity gradient across the arms in the $H\beta$ velocity field.

The general features of the CO velocity field are most clearly revealed by the $10''$ velocity field, shown in Figure 5. The lines indicate the major and minor axes derived by TA. The detected CO emission is entirely on the approaching (northeast) side of the galaxy. The southeast half of the galaxy is the far side under the assumptions in §I. Our fields include a location where the arms cross the major axis, allowing tangential streaming to be examined. The southern end of the detected arm is close to the minor axis, but the emission is very weak and covers a small across-arm width. Hence, an examination of radial streaming is much more difficult.

We first note that there is in general a sharp decrease in observed velocity (translating to an increase in tangential velocity) across the arm near the major axis. The rate of decrease is even higher in the full-resolution velocity field. This gradient could be due to either tangential streaming or a rising rotation curve. TA did in fact derive a rising curve from their HI data, but the slope is much too small to explain the gradient. On the approaching side, they find V_{rot} increases in this radial range by about 10 km s^{-1} over $20''$ (the approximate width of the detected CO arm near the major axis), or 4 km s^{-1} in the plane of the sky. The observed gradient in Figure 5 is about $20\text{--}40 \text{ km s}^{-1}$. Hence, the CO shows rather strong tangential streaming in the sense expected (e.g. Roberts & Stewart 1987) for gas flowing through a density wave compression. The gradient in the CO data varies somewhat along the arm, but is typically $120 \text{ km s}^{-1} \text{ kpc}^{-1}$ and $85 \text{ km s}^{-1} \text{ kpc}^{-1}$ in the full- and $10''$ -resolution CO velocity fields, respectively. The different gradients indicate that resolution is an issue, and it is possible that an even larger value would be observed at higher resolution. In contrast, TA found no evidence for strong streaming in their $12''$ -resolution $H\beta$ velocity field. Their data seem to be more dominated by velocity irregularities, which may mask more regular streaming motions.

At locations close to the minor axis on the far side, the radial inflow of gas as it passes through the compression should be manifested as an observed velocity decrease from the front to the back of the arm. No such trend is clear in Figure 5, but for reasons stated above, one may not

expect such a gradient to be seen in our data.

3.5. Surface Density Contrasts and Gravitational Instability

The tangential velocity gradient can be used to show how the usual shear associated with a flat rotation curve is modified in a spiral arm (e.g. Elmegreen 1994; Rand 1993b, 1995). The rate of shear is given by the Oort A constant:

$$A = 0.5 \left(\frac{v}{R} - \frac{\partial v}{\partial R} \right) \quad (3)$$

The rotation speed at $R = 2.3$ kpc is 140 km s^{-1} (TA). For the case of no streaming and using the slightly rising rotation curve of TA (see §3.3), $A = 20 \text{ km s}^{-1} \text{ kpc}^{-1}$. $A = 0 \text{ km s}^{-1} \text{ kpc}^{-1}$ corresponds to local solid-body rotation. For the tangential velocity gradient of $120 \text{ km s}^{-1} \text{ kpc}^{-1}$ measured from the full-resolution velocity field, A becomes $-30 \text{ km s}^{-1} \text{ kpc}^{-1}$. The negative value indicates that the shear in the arms is prograde: gas at the back of the arms has a higher orbital angular frequency than gas at the front. This situation should reverse itself in the interarms (as observed in M51; Rand 1993b), but we cannot test this because we have not detected any interarm CO emission.

The tangential streaming, if it is measurable, can also be used to estimate the spiral arm surface density enhancement in the molecular gas. This dynamical method, based on Balbus & Cowie (1985), has been applied to the grand-design spirals M51 (Rand 1993b) and M100 (Rand 1995), and avoids the issue of whether CO emission traces molecular mass in the same way in both arm and interarm regions. The method assumes a tightly wound spiral in which mass and angular momentum are conserved as the gas flows in and out of the arms. In this case, the local “effective” epicyclic frequency (different in the arm, interarm, and axisymmetric case because of its dependence on streaming motions) of the gas varies with the local surface density, and it can be shown that the ratio of arm to axisymmetrically averaged surface densities is given by:

$$\frac{\Sigma_{\text{arm}}}{\Sigma_{\text{axi}}} = \frac{\kappa_{\text{arm}}^2 / \Omega_{\text{arm}}}{\kappa_{\text{axi}}^2 / \Omega_{\text{axi}}} = \frac{1 + \frac{R}{v} \left(\frac{\partial v}{\partial R} \right)_{\text{arm}}}{1 + \frac{R}{v} \left(\frac{\partial v}{\partial R} \right)_{\text{axi}}} \quad (4)$$

where κ is the effective epicyclic frequency, and v is the tangential speed at galactocentric radius R . Note that this method is independent of errors in the distance to the galaxy or its inclination. Using the above gradient of $120 \text{ km s}^{-1} \text{ kpc}^{-1}$ and the rotation curve of TA at this radius, $\frac{\Sigma_{\text{arm}}}{\Sigma_{\text{axi}}} \approx 2.3$. Lord (1987) found that the azimuthally averaged molecular surface density at $R = 2.3$ kpc, assuming $X = X_{\text{Gal}}$, is about $100 \text{ M}_{\odot} \text{ pc}^{-2}$. The molecular surface density in this part of the northern segment of the arm is then about $230 \text{ M}_{\odot} \text{ pc}^{-2}$.

The arm-interarm contrast will be greater than 2.3, but we cannot estimate it without a determination of interarm streaming gradients. However, it is interesting that Wiklind (1990), using SEST CO 1-0 and 2-1 data and a model with a composite of optically thin and thick

gas, derived a contrast somewhat further down the arm of at least 4.5 on 45'' scales. These two independent methods suggest that strong compression of the molecular gas occurs in M83 at this radius. In comparison, an arm-interarm contrast of 4 and an arm-axisymmetric contrast of 2 were found for M51 at around $R = 3$ kpc, while values of 2-3 and 1.5 were found for M100 near $R = 5$ kpc. The derived arm surface density is somewhat higher than in M51 (140 and 170 $M_{\odot} \text{ pc}^{-2}$ for the two arms) and much higher than in M100 (60 $M_{\odot} \text{ pc}^{-2}$ in the northwest arm).

Finally, following Rand (1995), we use two different criteria for assessing whether the gas in the arms near the major axis crossing should be gravitationally unstable. The first is based on observations: Kennicutt (1989) finds that significant star formation in spirals occurs only above a surface density threshold related to the Toomre criterion for gravitational instabilities in a uniform gas disk (Safronov 1960; Toomre 1964; Quirk 1972):

$$\Sigma_c = \frac{\kappa \gamma^{1/2} c}{\pi G} \quad (5)$$

where Σ_c is the threshold surface density, γ is the ratio of specific heats, here chosen to be 0.5 (*e.g.* Elmegreen 1992), c is the one-dimensional gas velocity dispersion, and κ is the effective epicyclic frequency.

We use the value of κ used to evaluate Eq. (4) for the arm and $c = 8 \text{ km s}^{-1}$, the mean for the emission features. We find $\Sigma_c = 57 M_{\odot} \text{ pc}^{-2}$, well below the arm surface density derived above. The most uncertain observational input into this comparison is probably the value of X , which would have to be four times lower than assumed to make the gas in the arms marginally stable. The agreement of flux-based and virial masses for the structures along the arms suggests that this is unlikely if the structures have properties similar to Galactic GMCs.

The second criterion comes from a theoretical treatment of gravitational collapse in a shearing, magnetized spiral arm by Elmegreen (1994), and was applied to M100 by Rand (1995). The criterion describes whether an azimuthal (along the arm) instability can collapse before it emerges from the arm. We use the same form as did Rand (1995):

$$C = 0.5 Q_0^{-1.5} (\rho_s / \rho_0)^{1.75} (1 - e^{-\chi})^{1.5} \Omega / (\Omega - \Omega_P) > 1 \quad (6)$$

If $C > 1$, there is sufficient time for collapse. Q_0 is essentially the Toomre criterion for the axisymmetric case, and is 0.5 for the sound speed, rotation curve and axisymmetric surface density at $R = 2.3$ kpc used above. ρ_s is the gas density in the arms and ρ_0 is the axisymmetrically averaged gas density. We assume that the gas scale height does not change in the arms so that $\rho_s / \rho_0 = \Sigma_s / \Sigma_0$. The parameter $\chi = (2G\mu_s)^{1/2} / c$, where μ_s is the gas mass per unit length along the arm. The latter quantity is the gas surface density multiplied by the arm width. Since the OVRO observations rapidly lose sensitivity to emission on scales of 30'' or larger, it is likely that the arm is broader than observed. An upper limit comes from the fact that Wiklind (1990) did not resolve the arm with a 43'' beam. We set the arm width to 30'', but in reality any reasonable choice of arm width results in $e^{-\chi} \ll 1$. For the pattern speed, we adopt the value of Kenney &

Lord (1991) of $51 \text{ km s}^{-1} \text{ kpc}^{-1}$, derived by assuming that corotation of the bar is at 1.4 times the bar radius, or $145''$. While it is not clear that the bar and spiral should have the same pattern speed (Sellwood & Sparke 1988), the spiral arms do begin at the ends of the bar, as would be expected if arms and bar rotated as one pattern. At $R = 145''$, some of the characteristics of corotation can be seen (Kenney & Lord 1991): the HII regions in the eastern arm cross from the outside to the inside edge of the arm, while in the western arm, the dust lane crosses the arm and the density of HII regions decreases significantly.

Using these values we derive $C = 34$, which certainly implies gravitational instability. Can making reasonable changes to the parameters bring it below unity? The number is very insensitive to the value of χ . Also, the velocity dispersion is reasonably well determined and is unlikely to contribute much uncertainty to the calculation. Uncertainty in the arm surface density has a much more dramatic effect on C through Q_0 : e.g. doubling the conversion factor, X , lowers C by a factor of 2.8. Halving the pattern speed (although there is no observational reason to do so) brings it down by a factor of 3.7. Changing the inclination to 14° will increase κ , and thus Q_0 , by a factor of 1.7, lowering C by a factor of 2. Finally, depending on the balance of the velocity dispersion and the gravity in the arms, the assumption of an unchanging scale height as the gas passes through the arms may not be true. If the scale height were doubled in the arms (presumably due to stirring by star formation activity), C would decrease by 3.4. Taken together, these four changes would lower C to 0.5, but this combination of circumstances is very unlikely and we conclude that the gas is indeed gravitationally unstable in the arms at around this galactocentric radius.

Although the comparison cannot be made for a broad range of galactocentric radii, it is interesting that these instability criteria are much more easily satisfied in M83 than in M51 or M100, suggesting that gas is more prone to gravitational collapse in this galaxy. As discussed in §1, M83 also has the highest surface density of star formation and a global star formation efficiency about three times as high as in M51, subject to uncertainties in X . The results are therefore suggestive of a link between star formation activity and efficiency and the degree to which the gas is gravitationally unstable to collapse.

4. Discussion – The CO Spiral Arm Morphology

The CO morphology in relation to the other spiral tracers raises as many questions as it answers. Neither the dust lane nor the young stars (as seen in a blue image) nor the non-thermal emission shows a very good coincidence with the CO emission over the entire mapped length of the arm. The similarity in spatial relationships with the western arm of M100 mentioned above suggests that there may be a common physical process responsible for this state of affairs.

The three possible explanations we consider for this morphology – UV heating, cosmic ray heating, and a two-component molecular phase – have their pros and cons, and show the need for further observations and theoretical work:

1) UV heating. One can argue that the CO-dust correlation is good in the northern segment because the dust lane is sufficiently clumpy, allowing the emission to be detected interferometrically. The southern dust lane is too smooth, and so CO is seen mostly near star forming regions due to a combination of sufficient column density and heating by stars. In both segments, most of the brightest HII regions are associated with the CO arm. The small-scale CO-H β correlation need not be perfect because a) some CO emission features may trace gas which has not yet formed many stars, b) some H β peaks may represent regions where massive stars have dispersed or dissociated the molecular gas, and c) H β should not trace star formation perfectly because of patchy extinction. The brighter HII regions in M83 indicate that stellar heating is more important than in M51. This scenario may not work so well in M100 since the bright end of the HII region luminosity function (Knapen 1997) much more closely resembles that of M51 (Rand 1992) than that of M83 (Rumstay & Kaufman 1983; Kennicutt, Edgar, & Hodge 1989). It should be remembered, however, that LK concluded that stellar heating was insufficient to explain the CO morphology; that the southern ridge must represent the peak of the molecular gas distribution. Also, the agreement of virial and flux-based masses for most of the emission features, if they are bound, suggests that CO emission traces molecular gas column density reasonably well and thus no strong additional source of heating is indicated.

2) Low-energy cosmic ray heating. For this mechanism to apply, the emission should correlate best with the non-thermal radio continuum. In favor of this explanation is the shift of both the CO and 20-cm continuum arms away from the dust lane in the southern segment. On small scales however, the correlation is rather poor, and possible thermal contamination in the high-resolution 20-cm map hampers the comparison. Again, the mass estimates for the emission features do not suggest a strong source of additional heating. A high-resolution thermal-nonthermal separation using maps at 3.6, 6, and 20 cm rather than an H β image and a 20-cm map may be more robust and may change the small-scale correlation. The same should be done for M100. Also, the distribution of low-energy cosmic rays may not be fully reflected in the distribution of synchrotron emission.

3) Two-component molecular phase. In this explanation, we are seeing the reaction of such a medium to the density wave, as discussed in §1. This requires that the density wave response weakens with distance along the arm appropriately so that both diffuse and dense components are trapped at the shock front in the northern segment, but only the diffuse component in the southern segment. The same scenario would apply for M100, while in M51, the compression is strong enough over the large part of the disk mapped in CO to trap both components along the dust lanes. The very low fraction of single-dish flux detected in our fields is at least consistent with a prominent diffuse molecular medium in M83. Against this scenario, perhaps, is that the streaming motions and inferred surface density of molecular gas in the arms are similarly high in M83 (at least in the northern segment) and M51, and lower in M100. Does the compression weaken sufficiently in the southern arm segment of M83 to allow the dense component to pass through the shock? Unfortunately, we cannot measure streaming motions there with these data.

Further progress on this issue would be made from a comparison of arm-interarm contrasts in near-IR observations – assuming that the contribution of younger stars can be understood and removed – in M83, M51, and M100 as a function of galactocentric radius, and more sensitive kinematic measurements.

There is evidence for the existence of widespread diffuse molecular gas in the Milky Way (Polk et al. 1988) and nearby spirals (Young & Sanders 1986), and the observations of M33 by Wilson & Walker (1994) suggest how this diffuse gas can be largely missed in interferometric observations. Clearly, the detectability of diffuse gas with interferometers should depend on its column density, CO emissivity and the linear beam-size. Its behavior in a spiral density wave compression relative to denser clouds could be explored further in simulations of the reaction of a two-component medium to density waves of various strengths. The dense-diffuse balance will depend on the ease of dense cloud creation, shredding of dense clouds by the radiative and mechanical energy of star formation (e.g. Elmegreen 1992) and perhaps in the density wave compression, itself a possible source of heating (Thomasson, Donner, & Elmegreen 1991). One would like to understand the life-cycle of dense and diffuse gas as it passes in and out of a spiral arm.

In all three scenarios, more could be gained by mapping the other arms of M83 and M100 in CO emission, and comparing spiral tracers. Of course, some combination of these mechanisms may also be at work. Also, any theory of CO heating must explain why flux-based and virial mass estimates agree for most of the emission features discussed in §3.3, assuming they are bound.

Finally, a more realistic estimate of the distribution of extinction would help in interpreting the CO emission. The visual appearance of dust lanes is due not only to the dust column density but also the relative distribution of dust and stars. In the star-forming part of the arm, for example, it is possible that enough new stars sit above the dust layer to give the appearance that there is much less dust than is actually present. Trehwella (1997) shows that by using multi-band optical and near-infrared photometry along with IRAS or ISO maps of infrared emission, the inferred distribution of starlight and extinction can be very different from the impression given by, say, a blue image. Applied to NGC 6946, his technique reveals a smooth, two-armed extinction-corrected spiral pattern in blue light, in contrast to the patchy, four-armed pattern familiar from uncorrected blue images. A similar analysis for M83 could be very enlightening.

5. Conclusions

The main conclusions from this study are:

- 1) We have detected molecular spiral structure along the eastern arm of M83. The northern part of the molecular arm shows reasonably good coincidence with the dust lane, while the southern part is offset downstream from the dustlane and shows better coincidence with the arm of young stars, confirming the results of LK. A map of non-thermal emission shows a similar behavior, although the small- scale correspondence with CO emission is sometimes poor. There

is little evidence of a clear CO-H β offset, but the fact that the CO emission in the northern arm segment lies at the front of the H β arm is still evidence for triggering of star formation by the density wave compression. The CO-dust-star formation morphology is similar to that in the western arm of M100, but is different from that of M51, where the CO-dust coincidence is excellent.

2) Three scenarios have been examined to explain the relationship of CO emission with other spiral tracers. First, it may be that CO is detectable in the northern segment because the dust lane is sufficiently clumpy there, while a ridge of bright HII regions may contribute to CO excitation. In the southern segment, the dust lane is rather smooth and CO is seen in the star forming arm due to heating provided by young stars. Second, CO emission may trace the distribution of low-energy cosmic rays if they are responsible for heating CO molecules. Third, the morphology may be due to the reaction of a two-component molecular medium to the spiral density wave. None of these explanations is completely satisfactory given these new data. Further observations and theoretical work should help to distinguish between the possibilities.

3) An unusually low fraction of 2-5% of the single-dish flux is recovered in the interferometric maps. This may be due to the proximity of the galaxy combined with a prominent, smoothly distributed diffuse molecular medium which is completely missed in these observations.

4) Emission features have masses ranging from the largest GMCs in the Milky Way to the GMAs of M51. Masses based on CO flux and virial masses roughly agree, suggesting that, if these features are bound, the standard Galactic value of X is reasonable. If true, this result must be accounted for by any theory of the heating of the CO.

5) Strong tangential streaming, consistent with passage through a density wave compression, is observed where the molecular arm crosses the major axis. From the amplitude of the streaming, the enhancement in surface density of the arm over the disk average at that radius is about 2.3, and the gas surface density in the arms is about $230 M_{\odot} \text{ pc}^{-2}$. The arm-interarm contrast will be greater than 2.3. Two criteria for large-scale gravitational instabilities in the arms are satisfied much more easily in M83 than in M51 or M100. Enhanced gravitational collapse may be responsible for the relatively high surface density and global efficiency of star formation in M83.

We are very grateful to J. Cowan for providing the 20-cm uv data, E. Deutsch for the 10''-resolution non-thermal map, and R. Tilanus for the H β image,

REFERENCES

- Adamson, A. J. Adams, D. J., & Warwick, R. S. 1987, MNRAS, 244, 367
Adler, D. S., Allen, R. J., & Lo, K. Y. 1991, ApJ, 382, 475
Adler, D. S., Lo, K. Y., Wright, M. C. H., Rydbeck, G., Plante, R., & Allen, R. J. 1992, ApJ, 392,

- Allen, R. J., Atherton, P. D., & Tilanus, R. P. J. 1986, *Nature*, 319, 296
- Balbus, S. A., & Cowie, L. L. 1985, *ApJ*, 297, 61
- Brouillet, N., Kaufman, M., Combes, F., Baudry, A., & Bash, F., 1998, *A&A*, 333, 92
- Comte, G. 1981, *A&AS*, 44, 441
- Cowan, J. J., Roberts, D. A., & Branch, D. 1994, *ApJ*, 434, 128
- Deutsch, E. W. & Allen, R. J. 1993, *AJ*, 106, 1812
- de Vaucouleurs, G. 1979, *AJ*, 84, 1270
- de Vaucouleurs, G., de Vaucouleurs, A., Corwin, H. G., Buta, R. J., Paturel, G., & Fouqué, P. 1991, *Third Reference Catalogue of Bright Galaxies* (Springer, New York)
- Dufour, R. J., Talbot, R. J., Jensen, E. B., & Shields, G. A. 1980, *ApJ*, 236, 119
- Elmegreen, B. G. 1988, *ApJ*, 326, 616
- Elmegreen, B. G. 1992, in *Star Formation in Stellar Systems* ed. G. Tenorio-Tagle, M. Prieto & F. Sanchez (Cambridge Univ. Press), p 381
- Elmegreen, B. G. 1993, *ApJ*, 411, 170
- Elmegreen, B. G. 1994, *ApJ*, 433, 39
- Gruendl, R. A., Ph.D. thesis, University of Maryland
- Kenney, J. D. P., & Lord, S. D. 1991, *ApJ*, 381, 118
- Kennicutt, R. C. 1988, *ApJ*, 334, 144
- Kennicutt, R. C. 1989, *ApJ*, 344, 685
- Kennicutt, R. C., Edgar, B. K., & Hodge, P. W. 1989, *ApJ*, 337, 761
- Kennicutt, R. C. Tamblyn, P., & Congdon, C. E. 1994, *ApJ*, 435, 22
- Knapen, J. H. 1997, *MNRAS*, 297, 255
- Knapen, J. H., Beckman, J. E., Cepa, J., & Nakai, N. 1996, *A&A*, 308, 27
- Knapen, J. H., Cepa, J., Beckman, J. E., del Rio, M. S., & Pedlar, A. 1993, *ApJ*, 416, 563
- Kuno, N., Nakai, N., Handa, T., & Sofue, Y. 1995, *PASJ*, 47, 745
- Lord, S. D. 1987, Ph.D. thesis, University of Massachusetts
- Lord, S. D., & Young, J. S. 1990, *ApJ*, 356, 135
- Lord, S. D., & Kenney, J. D. P. 1991, *ApJ*, 381, 130
- Lord, S. D. 1987, PhD Thesis, University of Massachusetts
- Maloney, P., & Black, J. H. 1989, *ApJ*, 325, 389
- Nakai, N., & Kuno, N. 1995, *PASJ*, 47, 761

- Polk, K. S., Knapp, G. R., Stark, A. A., & Wilson, R. W. 1988, *ApJ*, 332, 432
- Quirk, W. J. 1972, *ApJ*, 176, L9
- Rand, R. J. 1992, *AJ*, 103, 815
- Rand, R. J. 1993a, *ApJ*, 404, 593
- Rand, R. J. 1993b, *ApJ*, 410, 68
- Rand, R. J. 1995, *AJ*, 109, 2444
- Rand, R. J., & Kulkarni, S. R. 1990, *ApJ*, 349, 43
- Rand, R. J., Kulkarni, S. R., & Rice, W. 1992, *ApJ*, 390, 66
- Rice, W. et al. 1988, *ApJS*, 68, 91
- Roberts, W. W., & Stewart, G. R. 1987, *ApJ*, 314, 10
- Rots, A. H. 1980 *ApJS*, 41, 189
- Rumstay, K. S., & Kaufman, M. 1983, *ApJ*, 274, 611
- Safronov, V. S. 1960, *Ann. d'Astrophys.*, 23, 979
- Sandage, A., & Tammann, G. A. 1987, *A Revised Shapley-Ames Catalog of Bright Galaxies, Second Edition*, Carnegie Institution of Washington publication 635, Washington, D. C.
- Sault, R. J., Teuben, P. J., & Wright, M. C. H. 1995, in *Astronomical Data Analysis Software and Systems IV*, ed. R. A. Shaw, H. E. Payne, & J. J. E. Hayes, *ASP Conf. Series* 77, 443
- Scoville, N. Z., & Sanders, D. B. 1987, in *Interstellar Processes*, ed. D. Hollenbach & A. Thronson (Dordrecht: Reidel), 21
- Sellwood, J. A., & Sparke, L. S. 1988, *MNRAS*, 231, 25
- Sempere, M. J., & Garcia-Burillo, S. 1997, *A&A*, 325, 769
- Suchkov, A., Allen, R. J., & Heckman, T. 1993, *ApJ*, 413, 542
- Talbot, R. J., Jensen, E. B., & Dufour, R. J. 1979, *ApJ*, 229, 91
- Taylor, C. L., & Wilson, C. D. 1998, *ApJ*, 494, 581
- Thomasson, M., Donner, K. J., & Elmegreen, B. G. 1991, *A&A*, 250, 316
- Tilanus, R. P. J. 1990, PhD Thesis, University of Groningen
- Tilanus, R. P. J., & Allen, R. J. 1993, *A&A*, 274, 70
- Tilanus, R. P. J., Allen, R. J., van der Hulst, J. M., Crane, P. C., & Kennicutt, R. 1988, *ApJ*, 330, 667
- Toomre, A. 1964, *ApJ*, 139, 1217
- Trewhella, M., PhD Thesis, University of Wales
- Vogel, S. N., Kulkarni, S. R., & Scoville, N. Z. 1988, *Nature*, 344, 402

- Wiklind, T. et al. 1990, A&A, 232, L11
Wilson, C. D. 1995, ApJ, 448, 97
Wilson, C. D., & Walker, C. E. 1994, ApJ, 432, 148
Young, J. S., & Sanders, D. B. 1976, ApJ, 302, 680

This preprint was prepared with the AAS L^AT_EX macros v4.0.

Fig. 1.— Channel maps from the $6.5 \times 3.5''$ resolution cube at 5.2 km s^{-1} spacing. Contour levels are $-0.18, 0.18, 0.36, 0.54$, and $0.72 \text{ Jy beam}^{-1}$. The center velocity is indicated in the upper left corner of each panel.

Fig. 2.— Contours of total CO emission in M83 at $6.5'' \times 3.5''$ resolution. Contour levels are 2.6, 5.2, 7.8, 10.4, and 13 Jy (beam) $^{-1}$ km s $^{-1}$. Numbers indicate emission features discussed in §3.3. The dashed outline indicates the half-power points of the mosaicked primary beam response. The FWHM beam size is shown in the lower left corner.

Fig. 3.— Top left: contours of total CO emission in M83 at $6.5'' \times 3.5''$ resolution overlaid on a color representation of a blue CCD image. Top right: contours of total CO emission overlaid on a color representation of the 20-cm continuum map at resolution matched to the CO map. Bottom left: contours of total CO emission overlaid on the H β image of Tilanus & Allen (1993) at $4''$ resolution. The truncation at the northeast edge of the H β image marks the edge of the field of view of the observation. Bottom right: a three-color representation of the spiral tracers CO (blue), 20-cm continuum (red), and H β (green). CO contour levels are as in Figure 2.

Fig. 4.— Contours of total CO emission at $6.5'' \times 3.5''$ resolution overlaid on a grey-scale representation of the map of non-thermal emission of Deutsch & Allen (1993). CO contour levels as in Figure 2.

Fig. 5.— Velocity field (first-moment map) from the $10''$ -resolution cube of CO emission shown as grey-scale with contours. Darker shading corresponds to higher velocities. Velocity contours are from 430 km s $^{-1}$ to 500 km s $^{-1}$ in steps of 5 km s $^{-1}$. The 450, 470, and 490 km s $^{-1}$ contours are shown in white. The solid and dashed lines represent the major and minor axes of the galaxy, respectively. The beam-size is shown in the lower left corner.

Table 1: General Parameters of M83

		Reference
Type	SAB(s)bc	de Vaucouleurs et al. (1976)
Right Ascension ^a (1950.0)	13 ^h 34 ^m 11.55 ^s	
Declination ^a (1950.0)	-29° 36' 42".2	Cowan et al. (1994)
Heliocentric Systemic Velocity	505 km s ⁻¹	Comte (1981)
Distance	5.0 Mpc	Kennicutt (1988)
Linear Scale	1" = 24 pc	
Inclination	24°	Talbot et al. (1979)
Position Angle of Major Axis	225°	Talbot et al. (1979)
HI Mass ^b	1.0 × 10 ⁹ M _⊙	Tilanus & Allen (1993)
H ₂ Mass within $R = 115''^{b,d}$	5 × 10 ⁹ M _⊙	Lord (1987)
H α Luminosity ^{b,c}	3.7 × 10 ⁴¹ erg s ⁻¹	Kennicutt, Tamblyn, & Congdon (1994)
FIR Luminosity ^b	1.3 × 10 ¹⁰ L _⊙	Rice et al. (1988)

^aCentral radio continuum source

^bScaled to $D = 5$ Mpc

^cAn extinction correction has been made by Kennicutt et al. (1994)

^dAssumes $X = 2.8 \times 10^{20}$ mol cm⁻² (K km s⁻¹)⁻¹

Table 2: Star Forming Properties of M83, M51, and M100

	M83	M51	M100	References
Distance (Mpc)	5.0	9.6	17.1	
$L_{H\alpha} (10^{41} \text{ erg s}^{-1})^a$	4.9	3.6	3.6	(1)
$M_{HI} (10^9 M_{\odot})$	1	5	4	(2) (3) (4)
$M_{H_2} (10^9 M_{\odot})^b$	5	16	16	(5) (6) (7)
$L_{H\alpha}/D_{25}^2 (10^{38} \text{ erg s}^{-1} \text{ kpc}^{-2})^c$	3.6	2.6	1.0	
$L_{H\alpha}/M_{H_2} (10^{31} \text{ erg s}^{-1} M_{\odot}^{-1})$	7.2	3.1	2.5	
$L_{H\alpha}/M_{HI+H_2} (10^{31} \text{ erg s}^{-1} M_{\odot}^{-1})$	6.0	2.4	3.1	

^aAn extinction correction has been made (see Kennicutt et al. 1994)

^bThe same value of X has been used for all galaxies (see text). The H_2 masses are for the inner 115'', 170'', and 200'' for M83, M51, and M100, respectively

^cIsophotal diameters from de Vaucouleurs et al. (1991), corrected for inclination

References. — (1) Kennicutt et al. 1994; (2) Tilanus & Allen 1983; (3) Rots 1980; (4) Knapen et al. 1993 (5) Lord 1987; (6) Kuno et al. (1995); (7) Sempere, & Garcia-Burillo (1997).

Table 3: Offsets from Nucleus and Map Noise Levels of Observed Fields

Field	R.A. offset (arcmin)	Dec. offset (arcmin)	1σ rms ^a (mJy beam ⁻¹)
1	-1.07	0.79	68
2	-1.54	0.34	57
3	-1.59	-0.33	52
4	-1.50	-0.91	45

^aFor 5.2 km s⁻¹ channels. 1 Jy (beam)⁻¹ = 4.0 K in the full-resolution maps

Table 4: Parameters of Emission Features

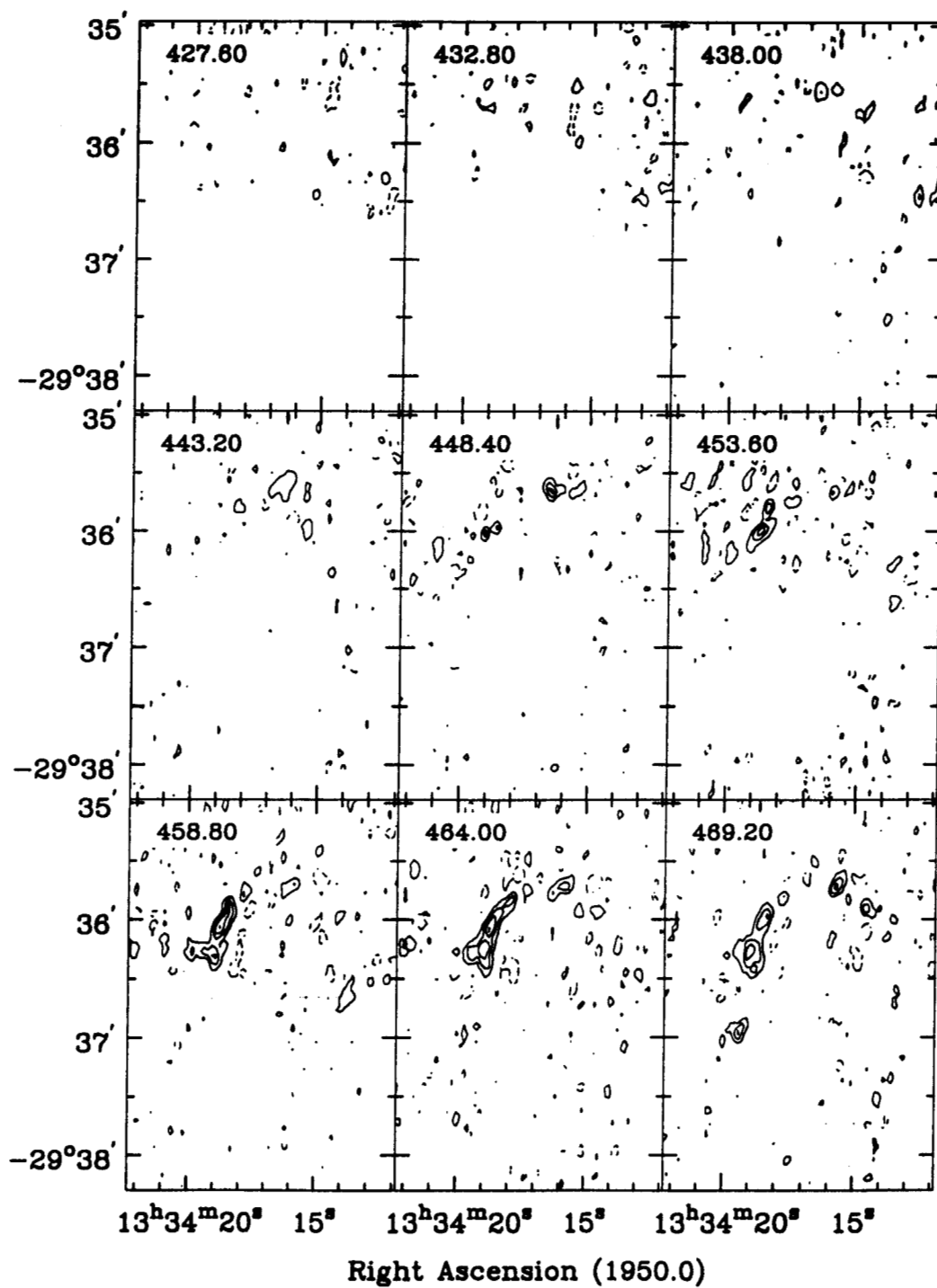
Feature	Offset from nucleus (arcmin)	M_{CO} ^a ($10^6 M_{\odot}$)	σ_{1d} ^b (km s^{-1})	$d_{\alpha} \times d_{\delta}$ (pc)	M_{vir} ($10^6 M_{\odot}$)	M_{vir} uncertainty ($10^6 M_{\odot}$)
1	(0.65,0.79)	2.3	6	140x150 ^c	<2.8	1.7
2	(0.82,0.76)	1.5	9	90x150 ^c	<5.2	2.8
3	(0.91,0.99)	6.6	8	200x150 ^c	<6.1	3.4
4	(1.03,0.97)	5.3	9	90x150	5.2	2.8
5	(1.08,1.12)	2.9	6	90x110	2.0	1.2
6	(1.54,0.69)	16	10	150x320	12	6.4
7	(1.61,0.42)	14	9	170x380	11	6.0
8	(1.51,0.26)	11	6	150x300	4.2	2.5
9	(1.69,-0.24)	7.3	6	120x270	3.6	2.2
10	(1.48,-0.20)	2.0	11	120x180	10	5.3

^aFractional uncertainty in M_{CO} is 0.8

^bTypical uncertainty in σ_{1d} is 2 km s^{-1}

^c d_{δ} is an upper limit

Declination (1950.0)



Declination (1950.0)

